3D PRINTING AND ADDITIVE MANUFACTURING
Volume 00, Number 00, 2022

DOI: 10.1089/3dp.2022.0062

Facile Adaptation of a Fused Deposition Modeling 3D Printer to Motionless Printing through Programmable Electric Relay: Discretized Modeling and Experiments

Sanjana Sham Sunder Bharadwaj, Chia-Yi Lin, Mounica J. Divvela, and Yong Lak Joo

Graphical Abstract

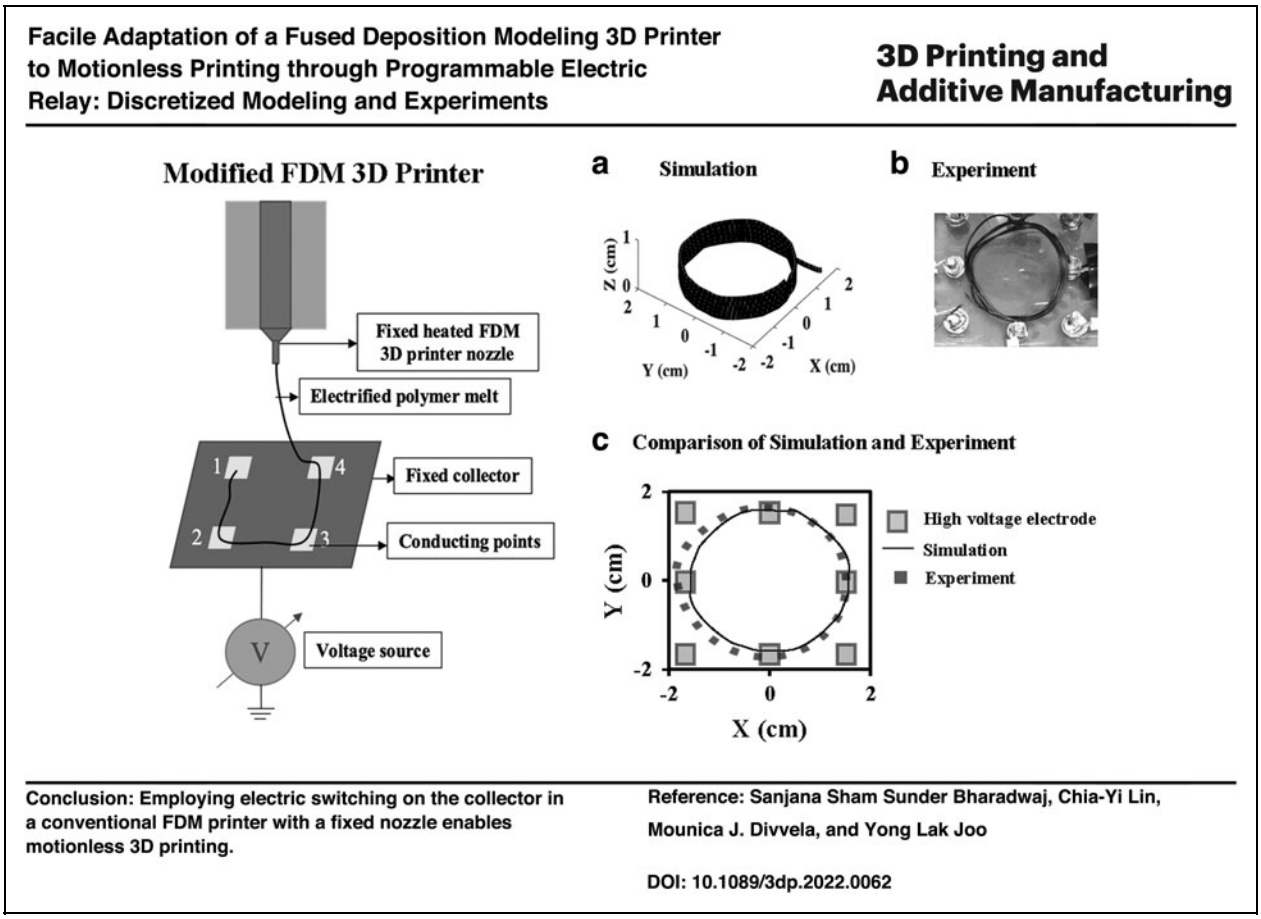

School of Chemical and Biomolecular Engineering, Cornell University, Ithaca, New York, USA.

Abstract

In this study, a fused deposition modeling 3D printer is modified into a motionless printer, which has the potential to print patterns in a noiseless manner possibly with improved resolution and in less delay time by eliminating the movement of nozzle or collector. In this motionless 3D printer, both nozzle and collector are fixed, whereas the extruded polymer melt is driven by high-voltage switching points on the collector. By this approach, simple 3D patterns such as multilayer circles, squares, and walls have been printed using two polymer melts with different rheological properties, high-temperature polylactic acid and acrylonitrile butadiene styrene. Furthermore, a discretized, nonisothermal bead and spring model is developed to probe printing patterns. The effect of parameters, such as number of conducting points, switching time, voltage and material properties on the accuracy of the printed simple 3D patterns, are thoroughly studied, and we demonstrated that various fiber collection patterns obtained from the experiments are favorably compared with the simulation results.

Keywords: motionless additive manufacturing, 3D printing, electrostatic field, EHD, discretized modeling

Introduction

FUSED DEPOSITION MODELING (FDM) printing is the most common 3D printing technology that deposits thermoplastic polymer melt coming out of the nozzle layer by layer onto a substrate by the motion of nozzle.[1,2] It has various applications in aerospace, automotive, biomedical industry, and consumer goods.[3–7] This FDM printing intrinsically involves some noise and delayed response time due to the movement of the nozzle head,[8–10] which can be curtailed if the printing can be done without the nozzle movement.

In the current work, FDM 3D printer is modified into a motionless printer by fixing the nozzle and collector. The melt polymer jets in this motionless printer are driven by high-voltage conducting points on the collector and their switching-in time. As opposed to conventional inkjet printers, jets driven by the electrical force can improve resolution and printing speed without miniaturizing nozzle because of a large neck-down ratio. The electric force driven, electrohydrodynamic inkjet printing allows producing submicron scale fibers with speed higher than 1 m/s. In some studies, the fiber dimension of printing patterns is no >20 μm.[11–13] In these studies, the Arduino is utilized to control the voltage switching time on the conducting points. Therefore, the printing speed can also be improved through the voltage switching time of the conducting points by revising the code in the Arduino. Besides, motionless 3D printing is not subject to whipping motion as seen in conventional solution electrospinning, and thus it allows for controlled deposition of jets[14] without using solvent.[15]

Compared with melt writing, another conventional printing technology, the current motionless printing approach, involves no movement: the nozzle and collector are fixed during the entire printing process and the printing trajectories are controlled by a designed pattern with the electric field. Therefore, it can potentially overcome the delay time of moving nozzle or collector and controls the fiber to reach the designed location quickly and precisely. The current motionless printing can be seen as an additive manufacturing process that bridges melt electrospinning and FDM 3D printing. It offers all the advantages of melt electrospinning, and thus eliminating the noisiness and potentially poor resolution, possibly with offering improved printing efficiency compared with FDM 3D printers.

In the current work, simple 3D patterns such as square, circle, and wall are printed in the motionless printer setup using acrylonitrile butadiene styrene (ABS) and high-temperature polylactic acid (HTPLA) melts with different rheological properties. The effect of switching time of electric field, voltage, and resolution (No. of conducting points) on simple 3D patterns is investigated experimentally. Discretized, nonisothermal bead and spring modeling is also developed to predict the pattern obtained. Several theoretical studies for electrospinning and melt electrospinning made use of solving series of coupled ordinary differential equations with Taylor cone-like analysis boundary.[16–19]

The bead and spring model is used for its computational rigor, with simplified equations of motion and energy to predict the pattern formed.[20–22] The modeling here is similar to the previous electrospinning model by Divvela *et al.*, but the nonisothermal effect on the molten polymer together with the energy balance and heat transfer at the fiber and air interface is also incorporated since the molten polymer undergoes cooling in air as the filament extruded from the heated nozzle.[21,23,24] A temporal boundary condition is applied to define the switching of voltage at the conducting points on the collector and these modeling results are then compared with printed patterns in experiments.[21]

Modeling Procedure

Motionless printing is modeled using the discretized nonisothermal bead and spring model. In this study, the polymer jet is assumed to be composed of a series of beads connected by springs in between them. The approach is similar to previously used immersed electrospinning system.[21] However, the medium is air here and nonisothermal effects are also incorporated into the model since the molten polymer jet undergoes cooling in air, as it is extruded from the heated nozzle and solidifies as it is deposited.

The radius r_i of each bead "i," with length l_i and mass m_i, as it flows from the nozzle is given by the conservation of mass equation, Equation (1).

$$r_i = \sqrt{\frac{m_i}{\rho \pi l_i}} \tag{1}$$

Each of the charged bead experiences forces such as surface tension $F_{st,i}$, aerodynamic force $F_{a,i}$, viscoelastic force $F_{v,i}$, electric force $F_{e,i}$, and gravitational force $F_{g,i}$. The

position of each bead "i" with position vector x_i, mass m_i, and radius a_i is obtained from Newton's second law of motion, given by Equation (2).

$$m_i\left(\frac{d^2\boldsymbol{x_i}}{dt^2}\right) = \boldsymbol{F_{st,i}} + \boldsymbol{F_{a,i}} + \boldsymbol{F_{v,i}} + \boldsymbol{F_{e,i}} + \boldsymbol{F_{g,i}} \quad (2)$$

The surface tension and viscoelastic force equations are taken from Divvela *et al.*[24] and Divvela and Joo.[23] The surface tension force is due to, (1) the capillary force along the jet axis and (2) force due to local curvature of the jet. In the surface tension equation, Equation (3), k_c is the local curvature of the jet and γ is the surface tension coefficient. *di* represents the downstream stream and *ui r*epresents the upstream beads with $\boldsymbol{e_{ui}}$ and $\boldsymbol{e_{di}}$ being the upstream and downstream unit vectors.

$$\boldsymbol{F_{st,i}} = \gamma\pi\left(\frac{a_{di}+a_{ui}}{2}\right)^2 k_c\left(\frac{\boldsymbol{e_{di}}+\boldsymbol{e_{ui}}}{|\boldsymbol{e_{di}}+\boldsymbol{e_{ui}}|}\right) + 2\pi\gamma(a_{di}\boldsymbol{e_{di}} - a_{ui}\boldsymbol{e_{ui}}) \quad (3)$$

The aerodynamic force by each bead $F_{a,i}$ is taken as an average of aerodynamic forces experienced by the upstream bead $F_{a,ui}$ and downstream beads $F_{a,di}$, given by Equation (4). The aerodynamic force experienced by upstream and downstream beads are given in Equations (5) and (6), respectively. The aerodynamic force is due to skin friction, $\boldsymbol{F_f}$ acting parallel to the axis of fiber, and pressure drag $\boldsymbol{F_p}$ acting normal to the fiber. ρ_{air} is the density of surrounding air and c_f and c_p are friction drag coefficient and pressure drag coefficient, respectively. V_t and V_n are tangential and normal velocity components of bead relative to air.

$$F_{a,i} = \frac{F_{a,ui} + F_{a,di}}{2} \quad (4)$$

$$\begin{aligned}\boldsymbol{F_{a,ui}} &= \boldsymbol{F_{f,ui}} + \boldsymbol{F_{p,ui}} \\ &= c_f\rho_{air}\pi a_{ui}l_{ui}|V_{t,ui}|\boldsymbol{V_{t,ui}} + c_p\rho_{air}a_{ui}l_{ui}|V_{n,ui}|\boldsymbol{V_{n,ui}}\end{aligned} \quad (5)$$

$$\begin{aligned}\boldsymbol{F_{a,di}} &= \boldsymbol{F_{f,di}} + \boldsymbol{F_{p,di}} \\ &= c_f\rho_{air}\pi a_{di}l_{di}|V_{t,di}|\boldsymbol{V_{t,di}} + c_p\rho_{air}a_{di}l_{di}|V_{n,di}|\boldsymbol{V_{n,di}}\end{aligned} \quad (6)$$

The viscoelastic force acting on bead "i" due to the upstream and downstream beads can be represented by Equation (7). τ_{di} and a_{di} represent the viscoelastic stress and radius of upstream bead, τ_{ui} and a_{ui} represent the viscoelastic stress and radius of the downstream bead, respectively.

$$\boldsymbol{F_{vi}} = \left(\pi a_{di}^2\tau_{di}\right)\boldsymbol{e_{di}} - \left(\pi a_{ui}^2\tau_{ui}\right)\boldsymbol{e_{ui}} \quad (7)$$

The viscoelastic stress of each bead τ_i has two components: (1) polymeric stress $\tau_{p,i}$ and (2) solvent stress $\tau_{s,i}$ as represented by Equation (8). Likewise, μ_s and μ_p represent the polymer and solvent contributions to polymer zero shear rate viscosity μ as shown in Equation (9). The viscoelastic stress is obtained from the nonisothermal Giesekus model,[24] Equations (8)–(12).

$$\tau_i = \tau_{p,i} + \tau_{s,i} \quad (8)$$

$$\mu = \mu_s + \mu_p \quad (9)$$

The solvent contribution of viscoelastic stress $\tau_{s,i}$ can be represented by Equation (10), where f_v is the temperature dependence on zero shear viscosity and $\frac{dl_i}{l_i dt}$ is the strain rate.

$$\tau_{s,i} = \mu_s f_v \frac{dl_i}{l_i dt} \quad (10)$$

The polymer contribution to viscoelastic stress $\tau_{p,i}$, is represented by Equation (11), where T_{ref} is the reference temperature, λ and α are the relaxation time and mobility factor of the polymer at the reference temperature obtained by fitting characterization results as shown in Table 1. f_v is calculated using Equation (12), where ΔH is the activation energy, obtained from calculations shown in Figure 1 and R_{ig} is the ideal gas constant.

$$\begin{aligned}&\tau_{p,i} + \lambda f_v\frac{T_{ref}}{T_i}\left(\frac{d\tau_{p,i}}{dt} - \tau_{p,i}\frac{1}{T_i}\left(\frac{dT_i}{dt}\right)\right) \\ &+ \alpha\frac{\lambda}{\mu_p}\frac{T_{ref}}{T_i}\tau_{p,i}^2 = \mu_p f_v\frac{dl_i}{l_i dt}\end{aligned} \quad (11)$$

$$f_v = \frac{\mu(T_i)}{\mu(T_{ref})} = \exp\left(\frac{\Delta H}{R_{ig}}\left(\frac{1}{T_i} - \frac{1}{T_{ref}}\right)\right) \quad (12)$$

The change in temperature of each bead dT_i is updated with respect to time using 1-D energy equation on fluid element in Equation (13). The energy balance consists of two elements: (1) viscous dissipation in the jet and (2) heat transfer with the surrounding air. C_p is the specific heat capacity, T_{air} is the temperature of surrounding air, and h is the heat transfer coefficient, which can be estimated using Kase–Matsuo's empirical formula as shown in Equation (14).[25]

$$\rho C_p\frac{dT_i}{dt} = \frac{\tau_i}{2}\frac{dl_i}{l_i dt} \quad (13)$$

Table 1. Material Properties of Acrylonitrile Butadiene Styrene Used in the Current Study

Properties	*Value*	*Source*
Zero shear viscosity at 220°C, η_0 (Pa·s)	12,849	Measured
Relaxation time, λ_1 (s)	158.3	Fitted
Activation energy of flow, $\Delta H/R_{\text{ig}}$ (K)	8340.9	Fitted
Density, ρ (kg/m^3)	1031	Ref.[26]
Specific heat, C_{p} (J/kgK)	1990	Ref.[27]
Electrical conductivity, K (S/m)	~10^{-15}	Ref.[28]
Surface tension, γ (N/m)	0.039	Ref.[29]
Mobility factor, α	0.008	Fitted
Ratio of solvent to zero shear viscosity, β	0.057	Fitted

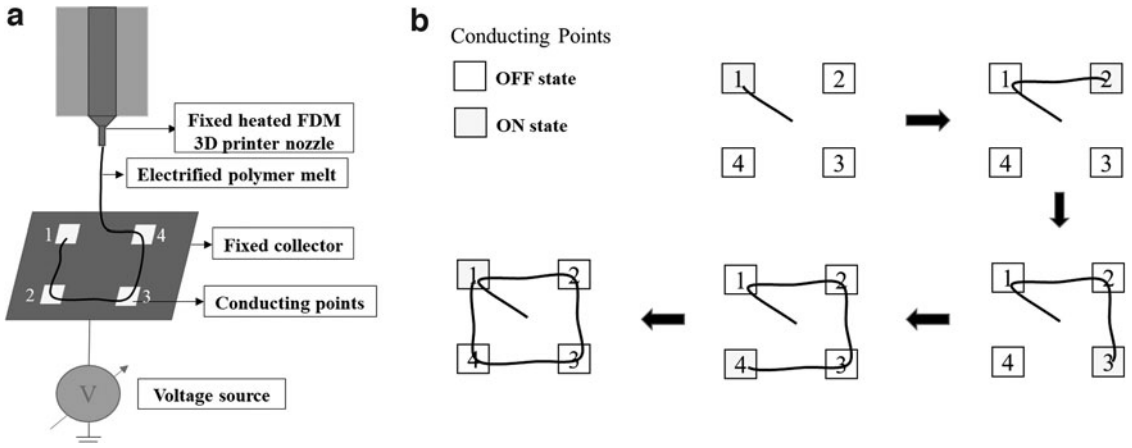

FIG. 1. **(a)** Schematic of an FDM 3D printer modified into a motionless 3D printer. **(b)** Schematic of pattern formed by voltage switching of conducting points. FDM, fused deposition modeling.

$$Nu = \frac{2a_i h}{k_{\text{air}}} = 0.495\left(\frac{2|V_t|a_i}{v_{\text{air}}}\right)^{\frac{1}{3}}\left(\frac{\rho_{\text{air}}C_{p,\text{air}}v_{\text{air}}}{k_{\text{air}}}\right)^{\frac{1}{2}}\left\{1+\left(\frac{8|V_n|}{|V_t|}\right)^2\right\}^{\frac{1}{6}} \quad (14)$$

In Kase–Matsuo's empirical formula, Nu is the Nusselt number, $C_{p,\text{air}}$, k_{air}, ρ_{air}, and v_{air} is the specific heat capacity, conductivity, density, and kinematic viscosity of air, respectively. ρ_{air} and k_{air} are functions of T_{air} and are calculated by Equations (15) and (16), respectively.

$$\rho_{\text{air}} = \frac{352}{T_{\text{air}}} \quad (15)$$

$$k_{\text{air}} = 1.879\times10^{-4}T_{\text{air}}^{0.866} \quad (16)$$

The electric field $\boldsymbol{E_{e,i}}$ is given by Equation (17) and has two components. The first term represents the diverging electric field experienced by the jet at distance "r_i" from the conducting points. The second term represents the coulombic interactions of bead "i" with the rest of the beads "j" at a distance $\boldsymbol{r_{ij}}$. Electric force is represented in Equation (18) where q_i is the charge at each bead.

$$\boldsymbol{E_{e,i}} = -\frac{2V_0}{\left(a_0+2r_i-\frac{r_i^2}{h_0}\right)}\boldsymbol{e_z} + \frac{1}{4\pi\epsilon_0}\sum_{j\neq i}\frac{q_j}{r_{ij}^3}\boldsymbol{r_{ij}} \quad (17)$$

$$\boldsymbol{F_{e,i}} = q_i\boldsymbol{E_{e,i}} \quad (18)$$

The charges are conserved by considering convection current only since conduction current is negligible for melt polymers with low conductivity. In addition, the leaky dielectric model is considered to get equilibrium value on surface of the jet, given by Equation (19). In this model, radial charge conduction is instantaneous since charges migrate quickly to the jet surface in fluids with low conductivity. Since the conductivity of melt polymer is negligible, conduction current is negligible and total current is equal to convection current.

$$q_i = 2\pi a\epsilon_0|E_{e,i}| \quad (19)$$

Experimental Procedure

Characterization of ABS and HTPLA

ABS and HTPLA solid linear polymers, whose diameters are 2.85 mm, are characterized using the DHR3 Rheometer to obtain some rheological parameters (Tables 1 and 2) that are used in the governing equations of nonisothermal discretized model as given in the Modeling Procedure section. The polymer is molten between the parallel plates in the rheometer and subjected to oscillatory shear at different temperatures to obtain the viscosity of the polymer as shown in Supplementary Figure S1 and S2. The ABS polymer has the viscosity of about two orders higher than HTPLA and it also exhibits some yielding behavior at low shear due to additives. Hence, the zero-shear viscosity of ABS is obtained by extrapolating the viscosity curve to mimic Cross model rheology. Other parameters, such as activation energy, relaxation time, zero shear viscosity, mobility factor, solvent, and

Table 2. Material Properties of High-Temperature Polylactic Acid Used in the Current Study

Properties	*Value*	*Source*
Zero shear viscosity at 220°C, η_0 (Pa·s)	614	Measured
Relaxation time, λ_1 (s)	8.3	Fitted
Activation energy of flow, $\Delta H/R_{\text{ig}}$ (K)	9006	Fitted
Density, ρ (kg/m^3)	1240	Ref.[30]
Specific heat, C_p (J/kgK)	1800	Ref.[31]
Electrical Conductivity, K (S/m)	$<10^{-10}$	Refs.[32,33]
Surface tension, γ (N/m)	0.0435	Ref.[34]
Mobility Factor, α	0.0085	Fitted
Ratio of solvent to zero shear viscosity, β	0.265	Fitted

polymer viscosity ratios of polymer melt, are obtained by fitting of the data to the Giesekus constitutive model Equations (20)–(22) as shown in Figure 1b and c.

In the Giesekus constitutive model, λ_1 is the relaxation time of the polymer, λ_2 is the retardation time, α is the mobility factor, and γ is the oscillatory shear strain. The fitted and measured rheological data of ABS and HTPLA melt are tabulated in Tables 1 and 2, respectively. These rheological data are used in modeling procedure in the Experimental Procedure section.

$$\frac{\eta}{\eta_0} = \frac{\lambda_2}{\lambda_1} + \left(1 - \frac{\lambda_2}{\lambda_1}\right) \frac{(1-f^2)}{(1+(1-2\alpha)f)} \tag{20}$$

$$f = \frac{1-\chi}{(1+(1-2\alpha)\chi)} \tag{21}$$

$$\chi = \frac{\left(1+16\alpha(1-\alpha)(\lambda_1\dot{\gamma})^2\right)^{\frac{1}{2}} - 1}{8\alpha(1-\alpha)(\lambda_1\dot{\gamma})^2} \tag{22}$$

Experimental setup

An existing Airwolf HD2x 3D printer is modified into a motionless printer, where the nozzle and collector are held stationary, and the molten jet is maneuvered using the high-voltage conducting points on the collector and their switching in time, as depicted in Figure 1a. To print a 3D square, four conducting points are arranged in four corners of a square and voltage is switched ON and OFF sequentially from point 1 to 4 to form a square pattern. First, point 1 is switched on until the polymer reaches the first conducting point. Next, point 1 is switched off and immediately point 2 is switched on until the polymer reaches point 2 and so on, until the pattern is completed, as shown in Figure 3b.

This switching of high voltage is controlled by a circuit, which is built using a combination of high-voltage DC supply, high-voltage relays, power switching MOSFET, Arduino, and conducting points. A detailed schematic of the electrical circuit is presented in Supplementary Figure S3. The timing and switching of high voltage supplied to conducting points can be controlled using Arduino codes.

In the current setup, screws, O-rings, or aluminum tapes are used as conducting points, which are arranged in a sequence depending on the 3D print pattern needed, with the nozzle centered above the conducting points. Patterns such as circles, squares, and 3D walls are printed using ABS and HTPLA experimentally with conditions mentioned in Table 3. Simulations are performed to gauge the appropriate initial conditions, such as voltage, switching time, number of conducting points etc. required to obtain an accurate pattern.

Results and Discussion

3D circle

Circle patterns for ABS and HTPLA were motionlessly 3D printed by using eight conducting points with the nozzle 4 and 8 cm centered above the collector, respectively, as shown in Figure 2a. The pattern was obtained by applying the equal voltage of 10 kV but unequal switching time across the conducting points, with the corner conducting points (CCP) being switched on for a shorter duration of 1 s and the middle conducting points (MCP) for 1.5 s. Simulations were conducted by applying the same initial conditions as the experiments, to obtain Figure 2b, and c shows the relation of conducting points switched ON/OFF with time. Since the CCPs were further away from the nozzle than the MCPs, the melt polymer experienced less electric field toward the CCPs. Hence, due to unequal switching time and unequal electric force experienced, the ABS melt extruded bypasses the corner points and took a curved path to touch only the MCPs forming a circle. It can be seen that the pattern predicted from discretized modeling simulation is close to the experimental results obtained (Fig. 2d).

Table 3. Typical Experimental Parameters Used in Motionless 3D Printing

Parameter	*Value*
Flow rate	2×10^{-8} m^3/s
Height from nozzle to collector	4 cm (ABS)
	8 cm (HTPLA)
Voltage	10 kV
Print temperature	220°C (ABS and HTPLA)
Radius of nozzle	0.5 mm

ABS, acrylonitrile butadiene styrene; HTPLA, high-temperature polylactic acid.

3D square

ABS 3D squares could be motionlessly printed using four conducting points in the four corners of a square at 4 cm distance from one another (Fig. 3a) with an equal voltage of 10 kV and an equal switching time of 2.3 s. Figure 3c shows the relation of conducting points switched ON/OFF with time. Experimental results show some warping of the jet in the regions between conducting points, whereas the simulation results predict an accurate square pattern.

As the number of conducting points are increased from four to eight, the accuracy of the printed pattern increases as shown in Figure 4. To obtain a square with eight conducting points, longer switching time was applied to CCPs. However, for the higher number of conducting points, it was harder to predict and control the switching time accurately causing it difficult to obtain an accurate multilayer pattern.

It was more difficult to print HTPLA than ABS since HTPLA had more fluid-like characteristics due to its lower viscosity. Squares were printed using a continuous conducting path made of aluminum tape to obtain pattern as shown in Figure 5a. A continuous path is comparable to a path with infinite conducting points. This further demonstrates that accurate patterns can be obtained with increased resolution. However, the conducting path in this experiment is 0.5 cm thick leading to slight misalignment in the multiple layers of the 3D square. These results are comparable with discretized modeling simulation results with four conducting points (Fig. 5b). The squares obtained from simulations have sharp edges, whereas the experiments lead to squares with rounded edges in both HTPLA and ABS. Possibly due to inertia, sharp

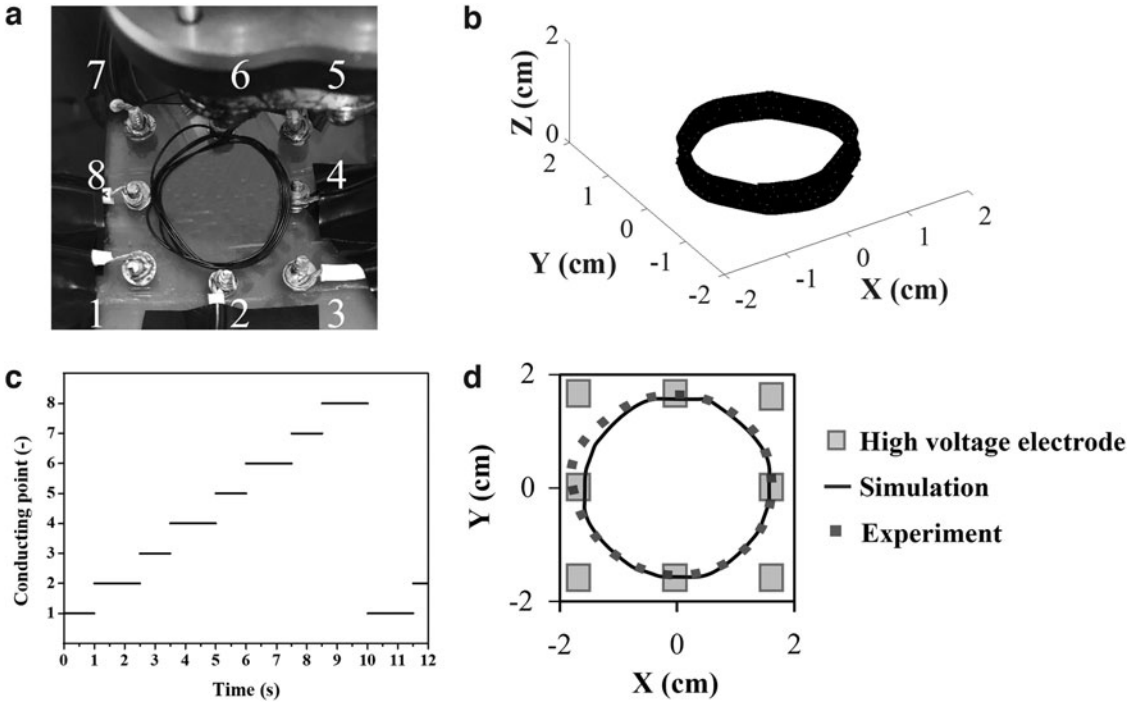

FIG. 2. Using eight conducting points with the nozzle. **(a)** Four centimeters above the collector formed ABS circle pattern in the experiment and **(b)** 8 cm above the collector formed HTPLA circular pattern in the simulation. **(c)** Shows how the conducting points switch with time in the first 12 s. **(d)** Shows the comparison on single layer ABS in the experiment and the simulation. The ''experiment'' figure was obtained by taking a picture of the stacked pattern from top view after the experiment was done and tracking it to scale using Adobe illustrator. ABS, acrylonitrile butadiene styrene; HTPLA, high-temperature polylactic acid.

edges are difficult to obtain experimentally, since the 3D printer has less flexibility to adjust the flow rate, while the discretized model is based on Stokes flow where inertial forces are assumed to be small compared with viscous forces. Reducing the melt polymer extrusion speed as the polymer approaches the edges can improve the results.

3D wall

HTPLA 3D stacked walls were printed perpendicularly layer by layer to the collector by using 2 O-rings as raised conducting points on the same axis, separated by 6 cm with a switching time of 3 s as shown in Figure 6a. There was slight

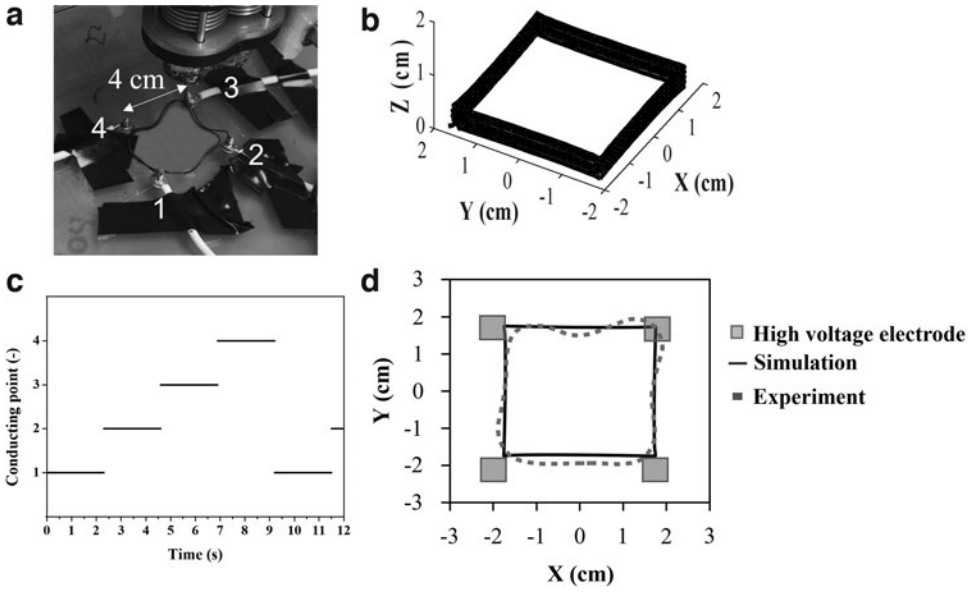

FIG. 3. ABS square pattern formed using four conducting points with the nozzle 4 cm above the collector in **(a)** the experiment and **(b)** the simulation. **(c)** Shows how the conducting points switch with time in the first 12 s. **(d)** Shows the comparison on single layer in the experiment and the simulation.

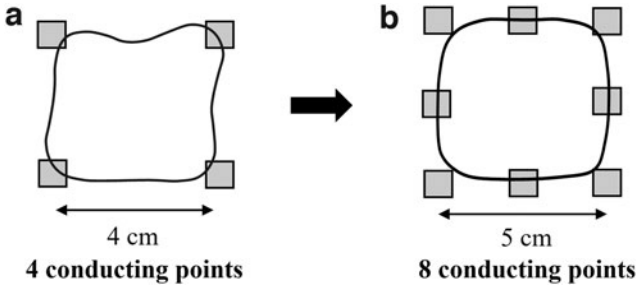

FIG. 4. ABS square pattern formed experimentally **(a)** with four conducting points and **(b)** with eight conducting points.

looping toward the end due to cooling of HTPLA fibers, but the pattern traced the same path each time. This demonstrates that highly repeatable patterns can be motionlessly 3D printed with accurate switching time and voltage. Simulation of HTPLA with two raised conducting points shows results, which are similar to the experimental results obtained (Fig. 6b).

Although the experimental results are in agreement with predicted simulation results, the accuracy of fiber deposition and alignment of subsequent layers in experiment are not perfect as simulation result due to the obstructing deposition by O-ring, quenching of polymer jet in the air, and the asynchrony between jet extrusion and switching of conducting points in the beginning. The detailed problems and the solutions in the experiment are explained point by point as follows: First, utilizing O-rings causes an obstruction of fibers near O-rings attaching the collector. However, raised conducting points (O-rings) lead to more accurate patterns since they guide the jet at an earlier stage in the air before it deposits onto the collector. Second, the polymer jet quenches in the air because of the high-temperature gradient between surrounding and nozzle causes decreasing electrical conductivity and hinders subsequent layers from fusing with the previous layer and form separate strands. Therefore, the fibers separate layer by layer slightly in Figure 6a and the lower electrical conductivity makes it more difficult to be guided by the electric fields.

To solve this problem, utilizing heater in the surrounding could help the jet cool down slowly and in better alignment of fibers due to the higher electrical conductivity of polymer fibers in its melt state. Third, the jet extrusion and switching of conducting points is asynchrony in the beginning. In the current set up, the voltage switches from one conducting

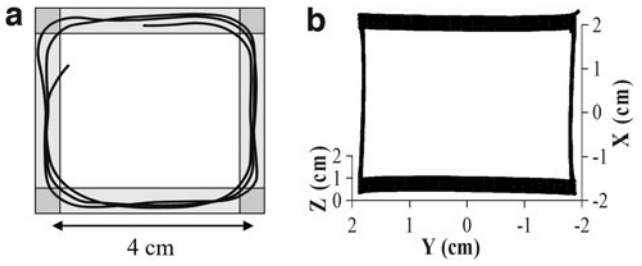

FIG. 5. HTPLA square pattern formed **(a)** experimentally with continuous conducting path and **(b)** through simulation with four conducting points.

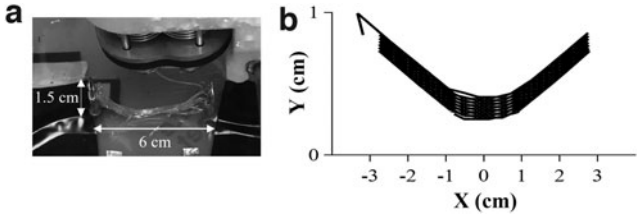

FIG. 6. HTPLA curved 3D wall pattern was printed perpendicularly layer by layer to the collector by using two conducting points **(a)** from experiments and **(b)** from simulation.

point to another in a constant loop as the fiber is extruded but they are asynchrony in the beginning. After one or two loops, the jets keep up themselves to the constant code of switching circuit. However, the initial nonaligning layers can act as a hindrance to accurate patterns being formed in the subsequent layers. So, the accuracy of deposition of fibers can be improved by coordinating extrusion of polymer with conducting point circuit using some motion sensors. Having a more sophisticated circuit with less delay time and greater resolution (more conducting points) can lead to deposition of patterns similar to the modeling results.

Effect of switching time, working distance, and voltage

Simulation results can be used to decide the experimental conditions to be applied to get accurate 3D print patterns. The modeling results in the section demonstrate the effect of parameters, such as switching time, working distance, and voltage strength for four conducting points (Fig. 7) and eight conducting points (Fig. 8).

Modeling results indicate that when switching time is low, for conducting points at optimized voltage of 10 kV as seen in Figure 7a, the fiber patterns do not reach the corners fully and are distorted. When the switching time is optimized, the melt jet effectively reaches the corners to form a defined square pattern (Fig. 7b). The modeling results, however, have smaller order of switching time since the delay or lag of equipments associated with experimentation is not taken into account.

Along with the distance and switching time between the conducting points, the distance from nozzle to the collector, working distance, also affects the printing pattern. From Figure 7c–e, it can be seen that, even when there is an insufficient electric field for fiber pattern formation, as the working distance increases, the polymer melt has more time to be electrified and maneuvered by the conducting points, making it reach the conducting points further.

The voltage is another important parameter in obtaining accurate printing patterns. It can be seen from Figure 7f–h that, as voltage decreases below 3 kV, the ability polymer deposited to reach the CCPs significantly decreases. For the square pattern deposition, conducting points were placed 4 cm away from each other and with 5 cm working distance. There was an agreement in the experimental results with the modeling when the same initial parameters were used, where it was observed that 3 kV acted as a sort of the threshold voltage for polymer fibers to be deposited onto the collector in a controlled manner. However, when voltage was increased beyond 10 kV, it was difficult for the polymer to

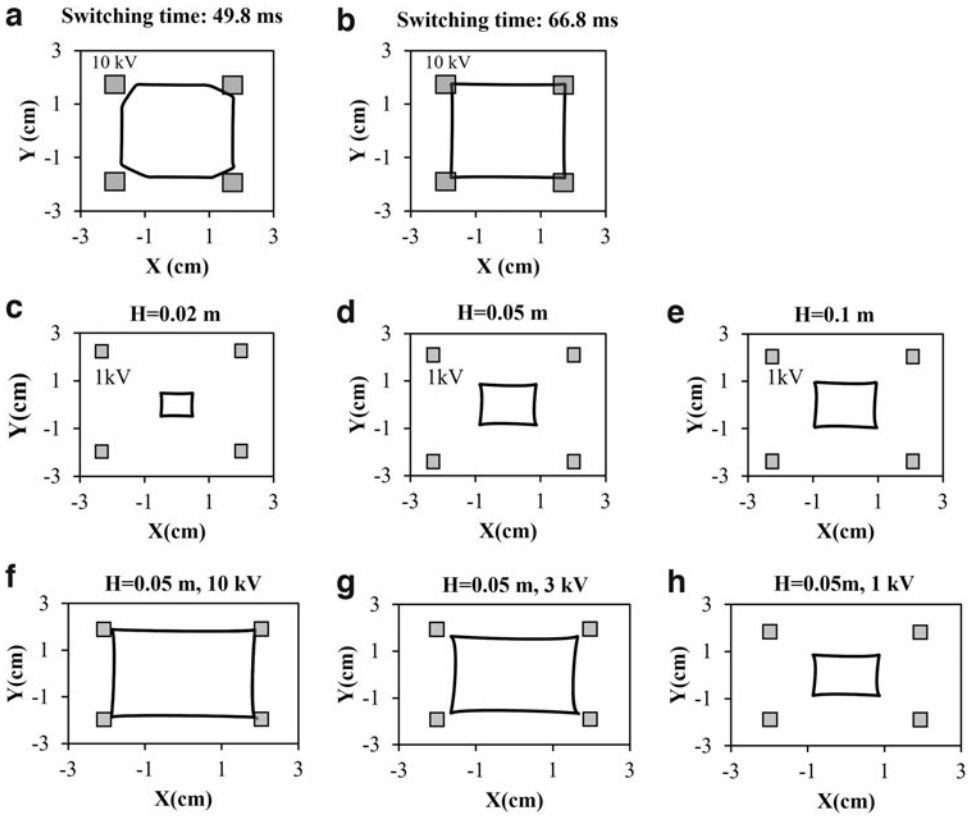

FIG. 7. ABS square pattern **(a)** and **(b)** formed from simulation of **(c)**, **(d)**, **(e)** four conducting points. *Top row*, **(f)**, **(g)**, **(h)** *middle row*, and *bottom row* show the printing patterns with different switching times, different working distances, and different voltages, respectively.

switch directions from one conducting point to another. The polymer fiber seemed to stick to a conducting point for a longer duration of 1 or 2 s, even after the conducting point was switched off, due to the residual charge in the polymer. The most optimal voltage for ABS pattern deposition was found to be between 8 and 10 kV and for HTPLA, a higher voltage of 10–14 kV was more effective.

The changed voltages also show the effect of the electric field, the voltage difference between nozzle and collector over the working distance, on the printing patterns. In the

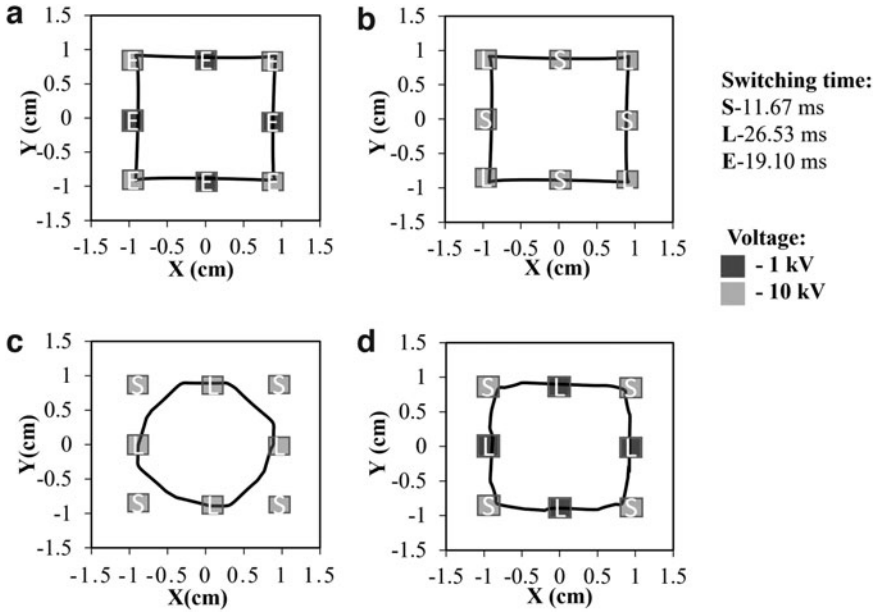

FIG. 8. ABS square pattern formed from simulation of eight conducting points with **(a)** equal switching time but higher voltage at corner conducting points, **(b)** equal voltage but longer switching time at corner conducting points, **(c)** equal voltage but shorter switching time at corner conducting points, and **(d)** shorter switching time and higher voltage at corner conducting points.

simulation cases as shown in Figure 7f–h, we applied 10, 3, and 1 kV to the conducting points with 5 cm working distance. The printing accuracy decreases with the decreasing electric field because of the changed voltages. If we want to get a higher printing accuracy of 3 and 1 kV as 10 kV, the lower working distances, 0.015 and 0.005 m, must need to be applied to the system, respectively. However, a short working distance must cause damage to the Rambo of the 3D printer, such as short circuit and spark problems.

Due to this high voltage requirement of 10 kV, distancing the working distance along with creating a heated environment around the extrusion area would be beneficial in obtaining better patterns and eliminating short circuit problems.

For eight conducting points, we can see from Figure 8a and b that perfect square can be obtained by two methods. One is applying higher voltage (10 kV) to the CCPs (point 1, 3, 5, 7) and lower voltage (1 kV) at the middle conduction points (2, 4, 6, 8) with the same switching time. The other is utilizing longer switching time (26.53 ms) at CCPs and shorter switching time (11.67 ms) at the MCPs with the same voltage. This implies that the best conditions getting a more accurate square in the experiment would be to apply longer switching time and higher voltage at CCPs while shorter switching time and lower voltage at MCPs. However, while the longer switching time is applied to MCPs instead of CCPs, circular pattern can be formed as shown in Figure 8c. Using this technique with unequal switching time in experiments shown in Figures 2 and 3 to obtain squares and circles works effectively. Another strategy that emphasizes the importance of unequal voltage is shown in Figure 8d, where although the switching time is longer at MCPs, the higher voltage at CCPs ''take over'' to ultimately form a square pattern.

We note that in the current study, we focused on the proof of concept of motionless 3D printing based on a facile adaptation of a FDM 3D printer by applying a programmable electric relay, and in the current motionless printing approach, the electric field that is applied at the bottom collector through conducting points decays rapidly as the height of printed 3D object increases. To apply the magnitude of the electrostatic field uniformly from the top of the 3D printed sample to the bottom, we are currently devising the voltage switching system near the collector where additional conducting points along both circumferential and horizontal directions are placed on additional wall around the 3D printing object.

Conclusion

In the current work, a motionless printer based on a fixed nozzle of a conventional FDM 3D printer with electric switching points on the collector is studied experimentally and theoretically. Simple 3D patterns such as circle, square, and wall were printed by using the electric force to drive the melt polymer jet. Discretized, nonisothermal modeling is also developed to study the motionless printer setup. This is done by incorporating energy balance equations to the bead and spring modeling to account for cooling of polymer jet after extrusion from the heated nozzle. In addition, the rheological behavior of this nonisothermal jet is modeled using nonisothermal Giesekus model.

Nonisothermal bead and spring modeling served as an effective tool to predict process conditions for the experiments. The effect of number of conducting points, switching time, working distance, and voltage was explored for various types of patterns to optimize the process. The model has been successful in predicting patterns formed by both ABS and HTPLA, which differ in relaxation time and viscosity by several orders. Three-dimensional circles were accurately printed using ABS and HTPLA with close comparison to the predicted modeling results. Three-dimensional squares, on the other hand, were more difficult to print but increasing the number of conducting points improved the accuracy of the 3D print. The HTPLA 3D wall proves that multilayer patterns tracing the same path can be printed with optimized voltage and switching time. Heated air around the printer, coordinating extrusion of polymer with the circuit, using close by conducting points with faster voltage switching system will be implemented to improve the alignment of 3D print patterns in motionless 3D printing.

To be able to print more complicated 3D objects in a motionless manner, however, more sophisticated ways of precisely controlling the electrostatic field on and around the jet and 3D objects must be implemented. In addition to adding a wall with circumferential and vertical points for the more uniform electrostatic field, modeling and experiments on a new motionless 3D printing system, where additional electric field is applied to the molten jet at the nozzle, are currently underway.

Authors' Contributions

S.S.S.B.: Investigation, Methodology, Software, Modeling, Design of Electrical Array, Printing Experiments, Visualization, Writing—Original Draft, and Writing—Review and Editing. C.-Y.L.: Investigation, Modeling, Printing Experiments, Writing—Original Draft, and Writing—Review and Editing. M.J.D.: Methodology, Software. Y.L.J.: Conceptualization, Funding acquisition, Writing—Review, Editing and Proofreading, and Supervision.

Acknowledgment

The authors would like to thank Shubha T.R. for help with the electrical connections.

Author Disclosure Statement

No competing financial interests exist.

Funding Information

This work made use of the Cornell Center of Materials Research (CCMR) Shared Facilities, which is supported through the NSF MRSEC program (DMR-1719875).

Supplementary Material

Supplementary Figure S1
Supplementary Figure S2
Supplementary Figure S3

References

1. Ngo TD, Kashani A, Imbalzano G, *et al.* Additive manufacturing (3D printing): A review of materials, methods, applications and challenges. Compos B: Eng 2018;143: 172–196.

2. Mwema FM, Akinlabi ET. Basics of Fused Deposition Modelling (FDM). In: Mwema FM, Akinlabi ET, eds. Fused Deposition Modeling: Strategies for Quality Enhancement. Cham: Springer International Publishing, 2020; p. 1–15. https://doi.org/10.1007/978-3-030-48259-6_1
3. Kalender M, Kılıç SE, Ersoy S, *et al.* Additive manufacturing and 3D printer technology in aerospace industry. In: 2019 9th International Conference on Recent Advances in Space Technologies (RAST), Istanbul, Turkey: IEEE, 11–14 June 2019.
4. Elakkad AS. 3D technology in the automotive industry. Int J Eng Res Technol 2019;8:248–251.
5. Ahangar P, Cooke ME, Weber MH, *et al.* Current biomedical applications of 3D printing and additive manufacturing. Appl Sci 2019;9:1713.
6. Kim S, Seong H, Her Y, *et al.* A study of the development and improvement of fashion products using a FDM type 3D printer. Fash Text 2019;6:9.
7. Liu Z, Wang Y, Wu B, *et al.* A critical review of fused deposition modeling 3D printing technology in manufacturing polylactic acid parts. Int J Adv Manuf Technol 2019;102: 2877–2889.
8. Belikovetsky S, Solewicz YA, Yampolskiy M, *et al.* Digital audio signature for 3d printing integrity. IEEE Trans Inf Forensics Secur 2019;14:1127–1141.
9. Dey A, Yodo N. A systematic survey of FDM process parameter optimization and their influence on part characteristics. J Manuf Mater 2019;3:64–93.
10. Miazio A. Impact of print speed on strength of samples printed in FDM technology. Agric Eng 2019;23:33–38.
11. Gao D, Zhou JG. Designs and applications of electrohydrodynamic 3D printing. Int J Bioprint 2019;5:172–182.
12. Zhang G, Qian L, Zhao J, *et al.* High-resolution electric-field-driven jet 3D printing and applications. 3D Print 2018. DOI: 10.5772/intechopen.78143.
13. Liashenko I, Rosell-Llompart J, Cabot A. Ultrafast 3D printing with submicrometer features using electrostatic jet deflection. Nat Commun 2020;11:753–761.
14. Góra A, Sahay R, Thavasi V, *et al.* Melt-electrospun fibers for advances in biomedical engineering, clean energy, filtration, and separation. Polym Rev 2011;51:265–287.
15. Muerza-Cascante ML, Haylock D, Hutmacher DW, *et al.* Melt electrospinning and its technologization in tissue engineering. Tissue Eng Part B Rev 2015;21:187–202.
16. Zhou H, Green TB, Joo YL. The thermal effects on electrospinning of polylactic acid melts. Polymer 2006;47: 7497–7505.
17. Zhmayev E, Zhou H, Joo YL. Modeling of non-isothermal polymer jets in melt electrospinning. J Nonnewtonian Fluid Mech 2008;153:95–108.
18. Mayadeo N, Morikawa K, Naraghi M, *et al.* Modeling of downstream heating in melt electrospinning of polymers. J Polym Sci B Polym Phys 2017;55:1393–1405.
19. Z Zhmayev E, Cho D, Joo YL. Modeling of melt electrospinning for semi-crystalline polymers. Polymer 2010;51: 274–290.
20. Liu B, Wang J, Fan X, *et al.* An effective bead–spring model for polymer simulation. J Comput Phys 2008;227: 2794–2807.
21. Divvela MJ, Frey MW, Joo YL. Discretized modeling of motionless printing based on retarded bending motion and deposition control of electrically driven jet. 3D Print Addit Manuf 2018;5:248–256.
22. Dasri T. Mathematical models of bead-spring jets during electrospinning for fabrication of nanofibers. Walailak J Sci Technol 2012;9:287–296.
23. Divvela MJ, Joo YL. Discretized modeling of beads-on-a-string morphology from electrically driven, conducting, and viscoelastic polymer jets. J Appl Phys 2017;121:134306.
24. Zhmayev Y, Divvela MJ, Ruo A-C, *et al.* The jetting behavior of viscoelastic Boger fluids during centrifugal spinning. Phys Fluids 2015;27:123101.
25. Matsuo T, Kase S. Studies on melt spinning. VII. Temperature profile within the filament. J Appl Polym Sci 1976; 20:367–376.
26. Tanikella NG, Wittbrodt B, Pearce JM. Tensile strength of commercial polymer materials for fused filament fabrication 3D printing. Addit Manuf 2017;15:40–47.
27. MatWeb—The Online Materials Information Resource. 2021. https://www.matweb.com/ (last accessed August 5, 2022).
28. Paz R, Moriche R, Monzón M, *et al.* Influence of manufacturing parameters and post processing on the electrical conductivity of extrusion-based 3D printed nanocomposite parts. Polymers 2020;12:733.
29. Raghavan V. Acrylics on Plastics. Just Paint. 2014. https://justpaint.org/acrylics-on-plastics/ (last accessed August 5, 2022).
30. Proto-pasta technical datasheet. https://www.proto-pasta.com/pages/technical-data-sheets (last accessed August 5, 2022).
31. Cicero J, Dorgan J. Physical properties and fiber morphology of poly(lactic acid) obtained from continuous two-step melt spinning. J Polym Environ 2001;9:1–10.
32. Shinyama K, Fujita S, editors. Study on the electrical properties of a biodegradable plastic. In: Proceedings of the 7th International Conference on Properties and Applications of Dielectric Materials (Cat No 03CH37417), Nagoya, Japan: IEEE, 1–5 June 2003.
33. Nakagawa T, Nakiri T, Hosoya R, *et al.* Electrical properties of biodegradable polylactic acid film. IEEE Trans Ind Appl 2004;40:1020–1024.
34. Biresaw G, Carriere CJ. Correlation between mechanical adhesion and interfacial properties of starch/biodegradable polyester blends. J Polym Sci B Polym Phys 2001;39:920–930.

Address correspondence to:
Yong Lak Joo
School of Chemical
and Biomolecular Engineering
Cornell University
Ithaca, NY 14853
USA

E-mail: ylj2@cornell.edu